

# Structure of native chromatin fibres revealed by Cryo-ET in situ

Received: 26 August 2023

Accepted: 28 September 2023

Published online: 10 October 2023

 Check for updatesZhen Hou<sup>1</sup>, Frank Nightingale<sup>1</sup>, Yanan Zhu <sup>1</sup>, Craig MacGregor-Chatwin<sup>2</sup> & Peijun Zhang <sup>1,2,3</sup> 

The structure of chromatin plays pivotal roles in regulating gene transcription, DNA replication and repair, and chromosome segregation. This structure, however, remains elusive. Here, using cryo-FIB and cryo-ET, we delineate the 3D architecture of native chromatin fibres in intact interphase human T-lymphoblasts and determine the in situ structures of nucleosomes in different conformations. These chromatin fibres are not structured as uniform 30 nm one-start or two-start filaments but are composed of relaxed, variable zigzag organizations of nucleosomes connected by straight linker DNA. Nucleosomes with little H1 and linker DNA density are distributed randomly without any spatial preference. This work will inspire future high-resolution investigations on native chromatin structures in situ at both a single-nucleosome level and a population level under many different cellular conditions in health and disease.

In eukaryotes, chromatin is a highly dynamic nucleoprotein complex that not only stores genetic information, but also participates in gene expression, DNA replication, and DNA repair. Chromatin can undergo drastic changes in structure and composition during the cell cycle and in response to various environmental and cellular signals<sup>1–5</sup>. The building block of chromatin is the nucleosome, which consists of a 147-base-pair DNA wrapped 1.65 times around an octamer of histones H2A, H2B, H3, and H4<sup>6–9</sup>. However, to accommodate a two-meter-long DNA string into a human nucleus of around 10  $\mu\text{m}$  in diameter<sup>10</sup>, nucleosomes must be further packed into higher-order chromatin structures.

There have been extensive studies on chromatin fibres and nucleosome compaction. Purified chromatin at low ionic strength can be seen as sparsely connected nucleosomes, presenting a 10-nm beads-on-a-string structure which further coils into compact 30-nm chromatin fibres in the presence of linker histone H1 under moderate ionic conditions<sup>11–15</sup>. There have been several models proposed for the 30-nm chromatin fibre based on in vitro studies, the two most prominent being the zigzag and solenoid models<sup>15–25</sup>. The zigzag model, also known as the two-start fibre model (including both the “helical ribbon” and “twisted crossed-linker” models) suggests that nucleosomes zigzag back and forth with relatively straight DNA linkers<sup>18–20,22,23</sup>. The solenoid

model, also known as the one-start fibre model, suggests a helical structure generated by nucleosomes stacking linearly along the helical axis, where the linker DNA is bent connecting adjacent nucleosomes<sup>17,21,25</sup>. Computer simulations have suggested the co-existence of both models as well as flexible disordered models in the nucleus<sup>26–30</sup>. Recent studies have also indicated that nucleosomes are highly mobile in chromatin and can form heterogeneous groups<sup>31–35</sup>. However, the existence of 30-nm chromatin fibres in the native nucleus has long been debated over the past decades, as no such defined fibres have been observed in intact cells under native conditions<sup>36–42</sup>. The structure of native chromatin fibres thus remains elusive.


In this work, we decipher in situ structures of nucleosomes and show how individual nucleosomes are organized into chromatin fibres within the intact frozen-hydrated T-lymphoblast CEM cell nucleus using cryo-focused ion beam (cryo-FIB) milling and cryo-electron tomography (cryo-ET).

## Results

### Chromatin fibres revealed in the intact nucleus

To visualise the chromatin, we generated very thin CEM cell lamellae containing the interphase nucleus by automated cryo-FIB milling, with

<sup>1</sup>Division of Structural Biology, Wellcome Trust Centre for Human Genetics, University of Oxford, Oxford, UK. <sup>2</sup>Diamond Light Source, Harwell Science and Innovation Campus, Didcot, UK. <sup>3</sup>Chinese Academy of Medical Sciences Oxford Institute, University of Oxford, Oxford, UK.

 e-mail: [peijun.zhang@strubi.ox.ac.uk](mailto:peijun.zhang@strubi.ox.ac.uk)

the thinnest lamellae about 80-90 nm thick. The reconstructed tomograms clearly resolve chromatin fibres and individual nucleosomes in the heterochromatin region close to the nuclear envelope (Fig. 1a–d, Supplementary Movie 1). The width of these fibres is variable, ranging from 20 to 50 nm (Figs. 1a, c, d and 2c). An array of nucleosomes was seen to display a similar structure as the *in vitro* reconstituted two-start zigzag complex (Fig. 1c, circle)<sup>23</sup> and *in vitro* sections of isolated chicken erythrocyte nucleus<sup>43</sup>. Moreover, individual nucleosomes can be identified flanking a DNA spine (Fig. 1d, yellow oval). Nearly naked, nucleosome-free DNA was also observed (Fig. 1d, yellow arrowhead), which continues as a chromatin fibre.

These direct observations from individual nucleosomes, together with the distributions of pairwise distances and angles between adjacent nucleosomes from a large population (Fig. 1f), indicate that the native chromatin fibres appear highly variable and flexible, and no uniform 30 nm fibre structure was observed.

#### In situ structures of nucleosomes in the native nucleus

Template matching using a featureless nucleosome model (EMD-26339 with a 40 Å low-pass filter)<sup>44</sup> resulted in 10,000 particles from 5 tomograms of the thinnest lamellae. After the removal of false positives by classification and manual inspection, the remaining 6790

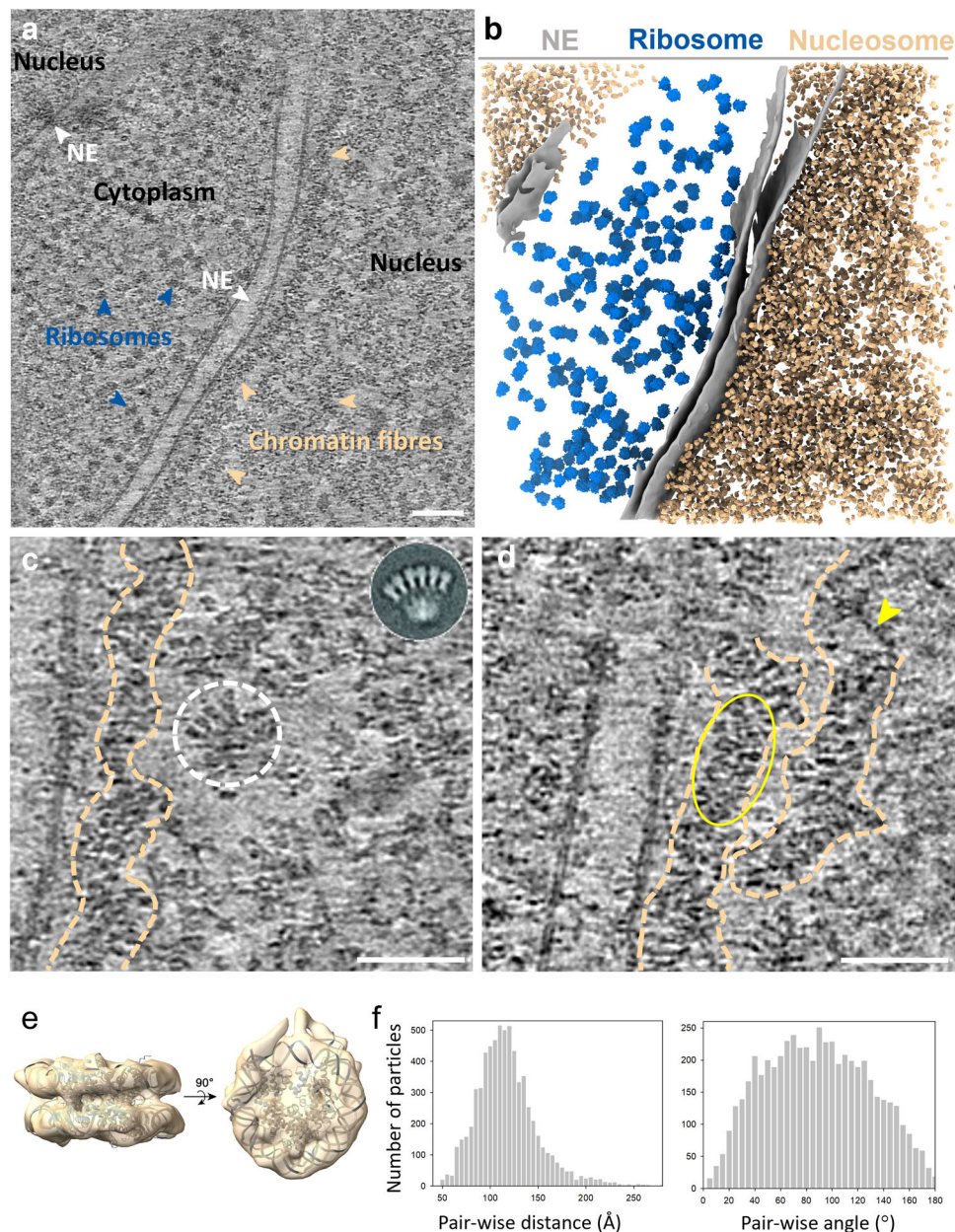


**Fig. 1 | Cryo-ET of native chromatin fibres and subtomogram average of nucleosomes.** **a** A representative tomographic slice of the CEM cell (from  $n = 5$ ). Scale bar = 100 nm. The tomogram is reconstructed with SIRT-like filtering in IMOD 4.11. The nucleus, chromatin fibres, nuclear envelope (NE), cytoplasm, and ribosomes are labelled accordingly. **b** The segmented volume of the tomogram in **a**. NE, ribosomes and nucleosomes are coloured grey, blue and gold, respectively. **c, d** Representative tomographic slices of chromatin fibres in the nucleus (from  $n = 5$ ). Prominent fibre structures are indicated by dash outlines. The white dashed

circle showcases a nucleosome array similar to the two-start zigzag structure of the reconstituted nucleosome complex (inset) (ref. 23). The yellow arrowhead points to naked DNA and the yellow oval shows nucleosomes flanking a DNA spine. Scale bars = 50 nm. **e** In situ structure of native nucleosomes (from  $n = 6790$ ,  $n$  of tomograms = 5), fitted with a crystal structure of core nucleosome (PDB 6ESF), shown in two orthogonal views. **f** Distributions of pair-wise distances and angles between the nearest nucleosome neighbours (from  $n = 6790$ ,  $n$  of tomograms = 5).



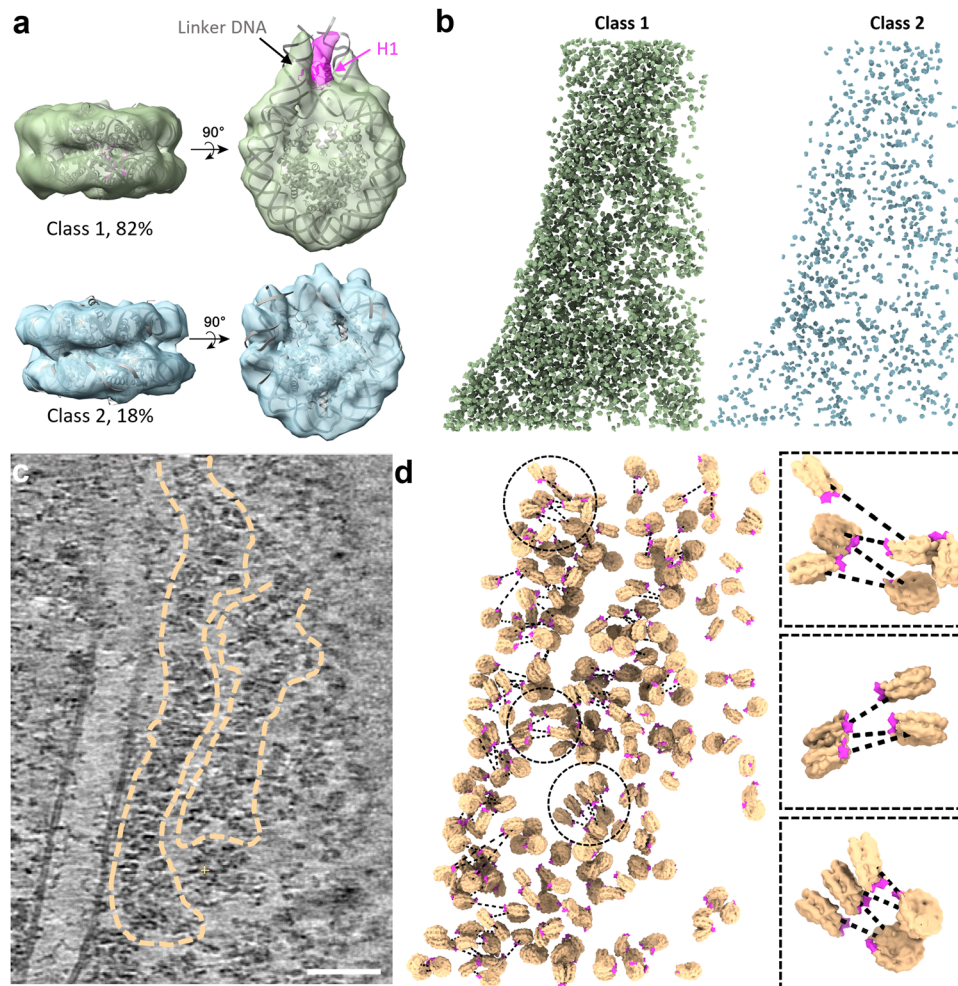


**Fig. 2 | 3D Organization of nucleosomes in native chromatin fibres.** **a** Two distinct classes of native nucleosomes. Class 1 (top) (82% of the total population,  $n = 5578$ ) is fitted with the nucleosome crystal structure PDB 7DBP, with H1 density coloured in magenta. Class 2 (bottom) (18% of the total population,  $n = 1212$ ) is fitted with the core nucleosome crystal structure PDB 6ESF. **b** Mapping back of individual nucleosomes from Class 1 (left) and Class 2 (right) into the representative

tomogram according to their coordinates and orientations. **c** A rotated tomographic slice (Y axis:  $-16^\circ$ , from Fig. 1d) depicting two clear chromatin fibres (dashed outlines). Scale bar = 50 nm. **d** Mapping back of individual nucleosomes in chromatin fibres in **c**. The H1 density is coloured magenta, indicating the side of entry and exit of the linker DNA, from which the DNA path (dashed lines) is predicted. Three representative sub-regions (circled) are enlarged on the right panel.

nucleosome particles were iteratively aligned and yielded a sub-tomogram average of the in situ nucleosome at 12.0 Å resolution (Fig. 1e, Supplementary Fig. 1a, b, Table 1, Supplementary Movie 2). The DNA dyads are clearly differentiated along with partial densities of the linker DNA and linker histone H1 (Fig. 1e). Further 3D classification of nucleosome particles resulted in two major distinct classes: class 1 (82%) shows a clear linker DNA density with partially resolved H1 globular domain (Fig. 2a, top), whereas class 2 shows little linker DNA and H1 density, suggesting these nucleosomes are likely more dynamic or flexible and perhaps have also lost H1 (Fig. 2a, bottom, Supplementary Fig. 1c, d). To test whether these two distinct populations of nucleosomes form special domains or prefer certain localization, we mapped each nucleosome from both classes back to the original tomogram. Intriguingly, the nucleosome particles from each class are distributed rather randomly without any spatial preference (Fig. 2b).

### 3D organization of nucleosomes in native chromatin fibres

The high quality of tomograms allowed the investigation of the architecture of native chromatin fibres. As the individual chromatin fibres can be delineated along with the nucleosomes in the original tomograms (Figs. 1c, d and 2c, marked with dashed lines, Supplementary Movie 3), we placed all identified nucleosomes back into the

fibre tomogram according to their refined positions and orientations (Fig. 2d). The nucleosome model used for the placement specifies the position of H1 and linker DNA (Fig. 2d, magenta), and thus allows the prediction of DNA paths and connection of adjacent nucleosomes (Fig. 2d, dashed black lines).

Within the fibres, the median distance between adjacent nucleosomes was measured at  $\sim 120$  Å, which is significantly larger than the expected distance (60–90 Å) calculated from the compact fibre models<sup>17–20,23,25</sup> (Fig. 3a). Moreover, when we divided nucleosomes into three subgroups of neighbouring distances, 60–80 Å, 80–100 Å, 100–120 Å, none of the nucleosome subpopulations showed a compact uniform fibre structure (Fig. 3b). Rather, all of them exhibited a flexible zigzag configuration. Consistently, the wide range of pairwise angles (Fig. 1f), and the distribution of nucleosome subpopulations with different ranges of angles (Fig. 3c), further support that the chromatin fibres are largely made of non-uniform, flexible zigzag-arranged nucleosomes. The calculated DNA concentration in our tomogram is approximately 15 mg/ml, which is consistent with the concentration of DNA within the nucleus ( $\sim 10$  mg/ml), suggesting the model is able to pack the entire genome into the nucleus. While the analysis of the overall nucleosome population does not suggest a uniform compact chromatin fibre, there are a few instances of short-

**Table 1 | CryoET data collection and structure determination of native nucleosomes**

Sample	T-lymphoblast CEM CD4+ cell lamellae
Microscope	FEI Titan Krios
Voltage (keV)	300
Detector	Gatan Quantum K3 Direct Electron Detector
Energy-filter	Yes
Slit width (eV)	20
Super-resolution mode	No
Physical pixel size (Å/pixel)	2.18
Defocus range (µm)	-3.5 to -5, increment 0.3
Acquisition scheme	Dose-Symmetric, -54/54, 3° step, group 3
Total dose (electrons/Å <sup>2</sup> )	111
Number of frames	10
Number of cells	5
Number of tomograms	5
<b>CryoET and subtomogram averaging</b>	
Number of subtomograms	6790
Resolution at 0.143 FSC cut-off (Å)	12.0
Data deposited	EMD-16978, EMD-16979, EMD-16980

ranged, partial compact nucleosomes (Figs. 1c and 2d), including dinucleosomes joined via interface 1 or interface 2<sup>23</sup> (Fig. 3d1-3), tetra- and poly-nucleosomes (Figs. 2d and 3d4-5).

## Discussion

The chromatin fibre and its structural model have been investigated and debated for many years. Using state-of-the-art cryo-FIB and cryo-ET, we revealed the elusive architecture of native chromatin fibres in intact cells without the drastic manipulation and harsh treatment of samples in previous studies<sup>35,45</sup>, and determined the in situ structure of nucleosomes at resolution of 12 Å, which is likely limited by the intrinsic dynamics and heterogeneity of native nucleosomes. The capacity to resolve linker DNA and linker histone H1, in partial, was critical to elucidating how nucleosomes are connected, and thus the structure of continuous chromatin fibres, which has not been possible in previous efforts<sup>31,32,35,42</sup>. Our data show that most nucleosomes are connected by straight linker DNA, forming a flexible, relaxed zigzag pattern, substantiated by both direct visualizations of individual nucleosomes and large-scale nucleosome population analysis. The architecture of the chromatin fibre determines the accessibility of the genome for transcription and other template-directed biological processes. Non-rigid chromatin fibre is likely beneficial for the effective tuning of the genome in response to varying protein expression and cellular stresses. This is also a reflection of dynamic chromatin with highly mobile nucleosomes<sup>31-35,42</sup>.

Chromatin per se constantly transforms during the entire cell cycle in response to various cell signalings<sup>1,4,5,42,46</sup>. While the structure of chromatin and chromatin fibres vary with cell types, cell states, nuclear positions, and signal perturbations, the fibre model we have postulated suggests a general mechanism for the compaction of the genetic material. The revelation of chromatin fibre structure in the interphase human nucleus opens a new avenue for future high-resolution in situ investigations of various native chromatin structures and their relevance to gene expression, the cell cycle, and stress responses.

## Methods

### Cell culture and vitrification

CEM CD4+ T-cells (catalogue ARP-117, HIV reagents program) were cultured in DMEM (Gibco) supplemented with 10% FBS, 2 mM L-glutamine (Gibco) and 1% MEM non-essential amino acids (Gibco), at

37 °C and 5% CO<sub>2</sub>. CEM cells at 3 × 10<sup>6</sup> cells/ml after 10 passages were pelleted at 200 × g for 5 min at 20 °C and resuspended in PBS mixed with 10% glycerol. An aliquot of 3 µl cell suspension was applied to the glow-discharged holey carbon-coated copper (R 2/1, 200 mesh) (Quantifoil) and blotted for 9 seconds by Leica GP2 (Leica Microsystems), followed by plunge freezing in liquid ethane.

### Cryo-FIB milling

Vitrified cells were further processed by cryo-FIB milling for the preparation of lamellae. A dual-beam microscope FIB/SEM Aquilos 2 (Thermo Fisher Scientific) equipped with a cryo-transfer system (Thermo Fisher Scientific) and rotatable cryo-stage cooled at -191 °C by an open nitrogen circuit was used to carry out the thinning. Prior to the milling, the grids were mounted on the shuttle and transferred onto the cryo-stage, followed by the coating with an organometallic Platinum layer using the GIS system (Thermo Fisher Scientific) for 5–6 s. Then, cells positioned approximately in the centres of grid squares were selected for thinning. The thinning was conducted by the automated milling software AutoTEM 5 (Thermo Fisher Scientific) in a stepwise manner from current 0.5 µA to 30 pA at 30 kV, and the final thickness of lamellae was set to 120 nm.

### Cryo-ET data collection

Cellular lamellae were transferred to FEI Titan Krios G2 (Thermo Fisher Scientific) electron microscope operated at 300 kV and equipped with a Gatan BioQuantum energy filter and post-GIF K3 detector (Gatan, Pleasanton, CA). A 100 µm objective aperture was inserted. Areas that include nuclei were selected for the data acquisition. Tilt series were recorded using Tomography 5 software (Thermo Fisher Scientific) with a nominal magnification of 42k and a physical pixel size of 2.18 Å/pixel. All tilt series were collected with a zero-loss imaging filter with a 20 eV-wide slit. The defocus value was set from -3.5 to -5 µm. The pre-tilt of the lamellae was determined at +9°, and a dose-symmetric scheme was applied for all tilt series, ranging from -45° to +63° with an increment of 3°. A total of 37 projection images with 10 movie frames each were collected for each tilt series and the dose rate was set at 1.5 e/Å<sup>2</sup>/s with an exposure time of 2 s, resulting in a total dose of 111 e/Å<sup>2</sup>. The correlated double sampling (CDS) in super-resolution mode was applied and frames were saved in LZW compressed tif format with no gain normalization. A total of 26 tilt series were collected from 22 lamellae.

### Alignment of tilt series and tomogram reconstruction

The frames of each tilt series were corrected for beam-induced motion using MotionCorr<sup>27</sup>. The gain correction was performed in parallel with the motion correction run by a home-brewed script. New stacks were generated and aligned using IMOD<sup>48</sup> version 4.11 by patch tracking, and tomograms were reconstructed at bin6 with a pixel size of 13.08 Å/pixel. For visualisation and segmentation, reconstructed tomograms were corrected for missing wedge and denoised by IsoNet<sup>49</sup> version 0.2, applying default parameters.

### Template matching

To localise individual nucleosomes in the tomogram, template matching was carried out using emClarity<sup>50</sup> version 1.5.0.2. To suppress the template-induced bias, a featureless nucleosome template was generated by low-pass filtering the published structure EMD-26339<sup>44</sup> to 40 Å. A total number of 5 tomograms with low residual errors in the alignment were selected for template matching, and 10000 particles in total were extracted. In parallel, ribosomes were picked using the low-pass-filtered structure EMD-16196<sup>51</sup>, and 200 particles were extracted from each tomogram for the segmentation.

### Subtomogram averaging

Prior to aligning the particles, CTF correction was performed for each tomogram by emClarity<sup>50</sup> version 1.5.3.10, and particles were checked



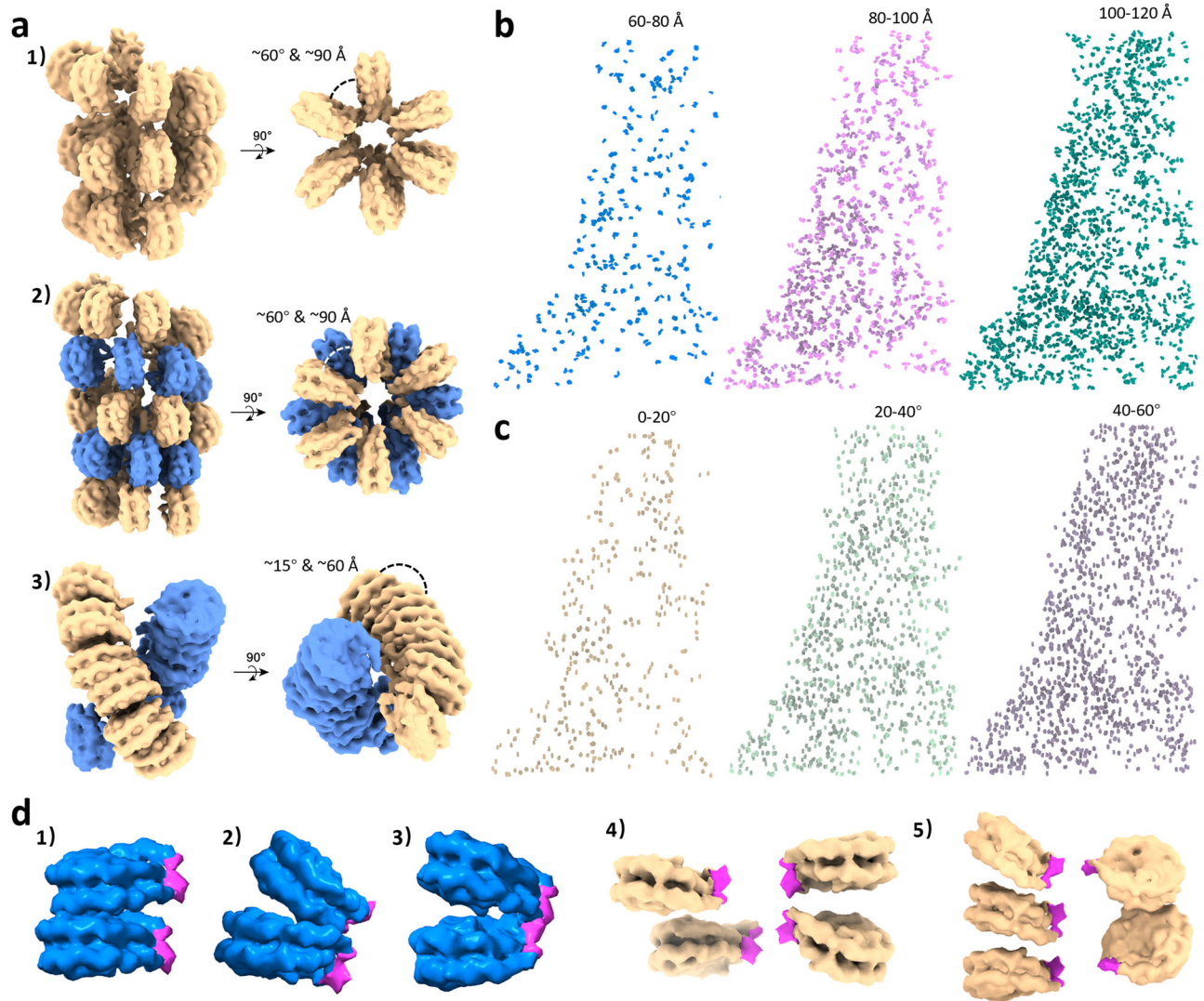


**Fig. 3 | Chromatin models and mapping of different subpopulations of the native nucleosome.** **a** Uniformed chromatin fibre models constructed based on previous works: (1) Ideal one-start solenoid model, (2) Ideal two-start twisted crossed-linker zigzag model, (3) EM-based compact two-start twisted zigzag model. The distance and angle between the neighboring nucleosomes are indicated. **b** Mapping back of three subpopulations of nucleosomes based on the nearest

neighbor distance: 60–80 Å (left), 80–100 Å (middle), 100–120 Å (right). **c** Mapping back of three subpopulations of nucleosomes based on the angle between the nearest neighbours: 0–20° (left), 20–40° (middle), 40–60° (right). **d** Examples of partial compact di-nucleosomes with type I (1) and type II interactions (2–3) (ref. 23), tetra- (4) and poly-nucleosomes (5) from the subpopulation of 80–100 Å in **b**. Partial densities of linker DNA and H1 are colored magenta.

by overlaying the reconstructed tomograms with corresponding picked particles in Chimera. Particles that lay outside the nucleus were then removed. The remaining particles were first aligned at bin6 and bin5 by emClarity version 1.5.3.10, followed by iterative reconstructions and alignments at lower binning (2–4) in RELION<sup>52</sup> version 4.0. To further clean up the particles, 3D classification was conducted at bin 6 in RELION<sup>52</sup> version 4.0, and 6,790 particles remained after the cleaning. The final resolution of the nucleosome was determined at 12.0 Å (0.143 cut-off). Using that structure as the reference, another round of 3D classification in RELION<sup>52</sup> was performed at bin6 with the number of classes set as 10. Class 1, 3, 4, 5, 6, 7, 8, and 9 showed prominent linker DNA densities while class 2 and 10 did not, thus particles from class 1, 3, 4, 5, 6, 7, 8, 9 were combined as one class (Class 1: 5,578 particles), particles from class 2 and 10 were combined as the other class (Class 2: 1,212 particles) (Supplementary Fig. 1c). These two classes were then aligned iteratively, and the final resolution of class 1 was determined at 12.5 Å (gold-standard 0.143 cut-off) (Supplementary Fig. 1b, blue line) while class 2 was resolved at 15 Å (gold-standard 0.143 cut-off). Map fitting was performed in ChimeraX<sup>53</sup>, and

the PDB 7DBP<sup>54</sup> and PDB 6ESF<sup>55</sup> were compared with class 1 and class 2, respectively.

#### Analysis of nucleosome population

The distance between adjacent nucleosomes was calculated according to the coordinates of their centres after the refinement. Paired nucleosomes with a centre-to-centre distance shorter than 60 Å were regarded as duplicates and removed. The angle between non-duplicate neighbouring nucleosomes was calculated using an in-house-developed script (<https://github.com/fnight128/MagpiEM>).

#### Segmentation and visualization

The segmentation was performed on IsoNet<sup>49</sup>-processed tomograms at bin6. The initial membrane detection and segmentation were done by TomoSegMemTV<sup>56</sup>, and the successive rendering was accomplished by ChimeraX<sup>53</sup>. Nucleosomes were mapped back according to their refined coordinates and orientations, using the subtomogram averaged nucleosome structure as the model. Ribosomes were mapped back to the tomogram as well, using a low-pass-filtered structure of

EMD-16196<sup>51</sup> (80 S human ribosome structure) as the model. Positions and orientations of ribosomes were based on the outputs from template matching.

### Reporting summary

Further information on research design is available in the Nature Portfolio Reporting Summary linked to this article.

### Data availability

The cryoET STA maps of in situ nucleosome structures in this study are available in the EMDB database under the accession codes EMD-16978 (Overall in situ H1-bound nucleosome structure with linker DNA), EMD-16979 (Class 1 in situ H1-bound nucleosome structure with linker DNA) and EMD-16980 (Class 2 in situ nucleosome structure without linker DNA).

### Code availability

The scripts used in this study and relevant codes are deposited in GitHub [<https://github.com/fnight128/MagpiEM>] and Zenodo [<https://doi.org/10.5281/zenodo.8362772>].

### References

- Hübner, M. R. & Spector, D. L. Chromatin dynamics. *Annu. Rev. Biophys.* **39**, 471–489 (2010).
- Brownell, J. E. et al. Tetrahymena histone acetyltransferase A: a homolog to yeast Gcn5p linking histone acetylation to gene activation. *Cell* **84**, 843–851 (1996).
- Joseph, M. The transition structure of chromatin fibers at the nanoscale probed by cryogenic electron tomography. *Nanoscale* **11**, 13783–13789 (2019).
- Pederson, T. Chromatin structure and the cell cycle. *Proc. Natl Acad. Sci. USA* **69**, 2224–2228 (1972).
- Raynaud, C. et al. Chromatin meets the cell cycle. *J. Exp. Bot.* **65**, 2677–2689 (2014).
- Kornberg, R. D. Chromatin Structure: a Repeating Unit of Histones and DNA: chromatin structure is based on a repeating unit of eight histone molecules and about 200 DNA base pairs. *Science* **184**, 868–871 (1974).
- Luger, K., Mäder, A. W., Richmond, R. K., Sargent, D. F. & Richmond, T. J. Crystal structure of the nucleosome core particle at 2.8 Å resolution. *Nature* **389**, 251–260 (1997).
- Oudet, P., Gross-Bellard, M. & Chambon, P. Electron microscopic and biochemical evidence that chromatin structure is a repeating unit. *Cell* **4**, 281–300 (1975).
- Zhou, M. et al. Structural basis of nucleosome dynamics modulation by histone variants H2A. B and H2A. Z. 2.2. *EMBO J.* **40**, e105907 (2021).
- Johnson, A., Lewis, J. & ALBERTS, B. Molecular biology of the cell. (2002).
- Kornberg, R. D. & Lorch, Y. Twenty-five years of the nucleosome, fundamental particle of the eukaryote chromosome. *Cell* **98**, 285–294 (1999).
- Olins, D. E. & Olins, A. L. Chromatin history: our view from the bridge. *Nat. Rev. Mol. Cell Biol.* **4**, 809–814 (2003).
- Takizawa, Y. & Kurumizaka, H. Chromatin structure meets cryo-EM: Dynamic building blocks of the functional architecture. *Biochim Biophys. Acta Gene Regul. Mech.* **1865**, 194851 (2022).
- Thoma, F., Koller, T. & Klug, A. Involvement of histone H1 in the organization of the nucleosome and of the salt-dependent superstructures of chromatin. *J. Cell Biol.* **83**, 403–427 (1979).
- Routh, A., Sandin, S. & Rhodes, D. Nucleosome repeat length and linker histone stoichiometry determine chromatin fiber structure. *Proc. Natl Acad. Sci. USA* **105**, 8872–7 (2008).
- Bednar, J. et al. Nucleosomes, linker DNA, and linker histone form a unique structural motif that directs the higher-order folding and compaction of chromatin. *Proc. Natl Acad. Sci. USA* **95**, 14173–14178 (1998).
- Finch, J. T. & Klug, A. Solenoidal model for superstructure in chromatin. *Proc. Natl Acad. Sci. USA* **73**, 1897–901 (1976).
- Woodcock, C., Frado, L.-L. & Rattner, J. The higher-order structure of chromatin: evidence for a helical ribbon arrangement. *J. Cell Biol.* **99**, 42–52 (1984).
- Schalch, T., Duda, S., Sargent, D. F. & Richmond, T. J. X-ray structure of a tetranucleosome and its implications for the chromatin fibre. *Nature* **436**, 138–41 (2005).
- Dorigo, B. et al. Nucleosome arrays reveal the two-start organization of the chromatin fiber. *Science* **306**, 1571–1573 (2004).
- Robinson, P. J., Fairall, L., Huynh, V. A. & Rhodes, D. EM measurements define the dimensions of the “30-nm” chromatin fiber: evidence for a compact, interdigitated structure. *Proc. Natl Acad. Sci. USA* **103**, 6506–6511 (2006).
- García-Saez, I. et al. Structure of an H1-bound 6-nucleosome array reveals an untwisted two-start chromatin fiber conformation. *Mol. Cell* **72**, 902–915 e7 (2018).
- Song, F. et al. Cryo-EM study of the chromatin fiber reveals a double helix twisted by tetranucleosomal units. *Science* **344**, 376–380 (2014).
- Dombrowski, M., Engeholm, M., Dienemann, C., Dodonova, S. & Cramer, P. Histone H1 binding to nucleosome arrays depends on linker DNA length and trajectory. *Nat. Struct. Mol. Biol.* **29**, 493–501 (2022).
- Widom, J. & Klug, A. Structure of the 300A chromatin filament: X-ray diffraction from oriented samples. *Cell* **43**, 207–13 (1985).
- Schlick, T. & Perišić, O. Mesoscale simulations of two nucleosome-repeat length oligonucleosomes. *Phys. Chem. Chem. Phys.* **11**, 10729–10737 (2009).
- Grigoryev, S. A., Arya, G., Correll, S., Woodcock, C. L. & Schlick, T. Evidence for heteromorphic chromatin fibers from analysis of nucleosome interactions. *Proc. Natl Acad. Sci.* **106**, 13317–13322 (2009).
- Collepardo-Guevara, R. & Schlick, T. Chromatin fiber polymorphism triggered by variations of DNA linker lengths. *Proc. Natl Acad. Sci. USA* **111**, 8061–8066 (2014).
- Bendandi, A., Dante, S., Zia, S. R., Diaspro, A. & Rocchia, W. Chromatin compaction multiscale modeling: a complex synergy between theory, simulation, and experiment. *Front. Mol. Biosci.* **7**, 15 (2020).
- Portillo-Ledesma, S. et al. Nucleosome clutches are regulated by chromatin internal parameters. *J. Mol. Biol.* **433**, 166701 (2021).
- Nozaki, T. et al. Dynamic organization of chromatin domains revealed by super-resolution live-cell imaging. *Mol. Cell* **67**, 282–293. e7 (2017).
- Lerner, J. et al. Two-parameter mobility assessments discriminate diverse regulatory factor behaviors in chromatin. *Mol. Cell* **79**, 677–688. e6 (2020).
- Nagashima, R. et al. Single nucleosome imaging reveals loose genome chromatin networks via active RNA polymerase II. *J. Cell Biol.* **218**, 1511–1530 (2019).
- Iida, S. et al. Single-nucleosome imaging reveals steady-state motion of interphase chromatin in living human cells. *Sci. Adv.* **8**, eabn5626 (2022).
- Ricci, M. A., Manzo, C., García-Parajo, M. F., Lakadamyali, M. & Cosma, M. P. Chromatin fibers are formed by heterogeneous groups of nucleosomes in vivo. *Cell* **160**, 1145–1158 (2015).
- Gan, L., Ladinsky, M. S. & Jensen, G. J. Chromatin in a marine picoeukaryote is a disordered assemblage of nucleosomes. *Chromosoma* **122**, 377–386 (2013).
- Cai, S. et al. Cryo-ET reveals the macromolecular reorganization of *S. pombe* mitotic chromosomes in vivo. *Proc. Natl Acad. Sci. USA* **115**, 10977–10982 (2018).

38. Cai, S., Böck, D., Pilhofer, M. & Gan, L. The in situ structures of mono-, di-, and trinucleosomes in human heterochromatin. *Mol. Biol. Cell* **29**, 2450–2457 (2018).
39. Fatmaoui, F. et al. Cryo-electron tomography and deep learning denoising reveal native chromatin landscapes of interphase nuclei. *bioRxiv*, 2022.08.16.502515 (2022).
40. Eltsov, M., MacLellan, K. M., Maeshima, K., Frangakis, A. S. & Dubochet, J. Analysis of cryo-electron microscopy images does not support the existence of 30-nm chromatin fibers in mitotic chromosomes in situ. *Proc. Natl Acad. Sci. USA* **105**, 19732–19737 (2008).
41. Chen, C. et al. Budding yeast chromatin is dispersed in a crowded nucleoplasm in vivo. *Mol. Biol. Cell* **27**, 3357–3368 (2016).
42. Maeshima, K., Ide, S. & Babokhov, M. Dynamic chromatin organization without the 30-nm fiber. *Curr. Opin. Cell Biol.* **58**, 95–104 (2019).
43. Scheffer, M. P., Eltsov, M. & Frangakis, A. S. Evidence for short-range helical order in the 30-nm chromatin fibers of erythrocyte nuclei. *Proc. Natl Acad. Sci. USA* **108**, 16992–7 (2011).
44. Weaver, T. M. et al. Structural basis for APE1 processing DNA damage in the nucleosome. *Nat. Commun.* **13**, 5390 (2022).
45. Ou, H. D. et al. ChromEMT: Visualizing 3D chromatin structure and compaction in interphase and mitotic cells. *Science* **357**, eaag0025 (2017).
46. Zhang, M. et al. Molecular organization of the early stages of nucleosome phase separation visualized by cryo-electron tomography. *Mol. Cell* **82**, 3000–3014. e9 (2022).
47. Zheng, S. Q. et al. MotionCor2: anisotropic correction of beam-induced motion for improved cryo-electron microscopy. *Nat. Methods* **14**, 331–332 (2017).
48. Kremer, J. R., Mastrorade, D. N. & McIntosh, J. R. Computer visualization of three-dimensional image data using IMOD. *J. Struct. Biol.* **116**, 71–76 (1996).
49. Liu, Y.-T. et al. Isotropic reconstruction for electron tomography with deep learning. *Nat. Commun.* **13**, 6482 (2022).
50. Himes, B. A. & Zhang, P. emClarity: software for high-resolution cryo-electron tomography and subtomogram averaging. *Nat. Methods* **15**, 955–961 (2018).
51. Berger, C. et al. Plasma FIB milling for the determination of structures in situ. *Nat. Commun.* **14**, 629 (2023).
52. Scheres, S. H. RELION: implementation of a Bayesian approach to cryo-EM structure determination. *J. Struct. Biol.* **180**, 519–530 (2012).
53. Goddard, T. D. et al. UCSF ChimeraX: meeting modern challenges in visualization and analysis. *Protein Sci.* **27**, 14–25 (2018).
54. Wang, S. et al. Linker histone defines structure and self-association behaviour of the 177 bp human chromatosome. *Sci. Rep.* **11**, 1–16 (2021).
55. Bilokapic, S., Strauss, M. & Halic, M. Histone octamer rearranges to adapt to DNA unwrapping. *Nat. Struct. Mol. Biol.* **25**, 101–108 (2018).
56. Martinez-Sanchez, A., Garcia, I., Asano, S., Lucic, V. & Fernandez, J.-J. Robust membrane detection based on tensor voting for electron tomography. *J. Struct. Biol.* **186**, 49–61 (2014).
- Hardenbrook for help with data analysis, and also acknowledge Dr. Long Chen for suggestions in statistical analyses. We acknowledge The Oxford Particle Imaging Centre (OPIC) for access to the cryo-FIB/SEM instrument (Aquilos 2) and Diamond Light Source for access and support of the cryo-EM facilities at the U.K. national eBIC (proposal NT29812), funded by the Wellcome Trust, MRC, and BBSRC. This research was supported by the UK Wellcome Trust Investigator Award (206422/Z/17/Z), the National Institutes of Health grants AI150481, the ERC AdG grant (101021133), and the Wellcome Trust Core Award Grant Number 203141/Z/16/Z with additional support from the NIHR Oxford BRC.

### Author contributions

P.Z. conceived the research. Z.H. and P.Z. designed the experiments. Z.H. and C.M. prepared the lamellae. Z.H. and Y.Z. collected data. Z.H. carried out tomography reconstruction and subtomogram averaging and classification. Z.H., F.N. and P.Z. analysed the data. Z.H. and P.Z. wrote the manuscript with help from all co-authors.

### Competing interests

The authors declare no competing interests.

### Additional information

**Supplementary information** The online version contains supplementary material available at <https://doi.org/10.1038/s41467-023-42072-1>.

**Correspondence** and requests for materials should be addressed to Peijun Zhang.

**Peer review information** *Nature Communications* thanks the anonymous reviewer(s) for their contribution to the peer review of this work. A peer review file is available.

**Reprints and permissions information** is available at <http://www.nature.com/reprints>

**Publisher's note** Springer Nature remains neutral with regard to jurisdictional claims in published maps and institutional affiliations.

**Open Access** This article is licensed under a Creative Commons Attribution 4.0 International License, which permits use, sharing, adaptation, distribution and reproduction in any medium or format, as long as you give appropriate credit to the original author(s) and the source, provide a link to the Creative Commons licence, and indicate if changes were made. The images or other third party material in this article are included in the article's Creative Commons licence, unless indicated otherwise in a credit line to the material. If material is not included in the article's Creative Commons licence and your intended use is not permitted by statutory regulation or exceeds the permitted use, you will need to obtain permission directly from the copyright holder. To view a copy of this licence, visit <http://creativecommons.org/licenses/by/4.0/>.

© The Author(s) 2023

### Acknowledgements

We thank Stanley Fronik for help in sample preparation, we thank Dr. Karen Davies for her support in data collection, we thank Dr. Nathan